

RESEARCH ARTICLE | FEBRUARY 09 2023

Digital twin of an apparatus for combined thermoelectric measurements

S. Kopatz ; P. Ziolkowski ; E. Müller

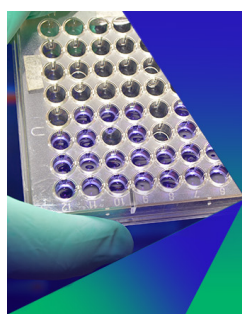


AIP Advances 13, 025036 (2023)

<https://doi.org/10.1063/5.0129504>



CrossMark



Biomicrofluidics

Special Topic:
Microfluidics and Nanofluidics in **India**

Submit Today



Digital twin of an apparatus for combined thermoelectric measurements

Cite as: AIP Advances 13, 025036 (2023); doi: 10.1063/5.0129504

Submitted: 3 November 2022 • Accepted: 19 January 2023 •

Published Online: 9 February 2023



S. Kopatz,^{1,a)} P. Ziolkowski,¹ and E. Müller^{1,2}

AFFILIATIONS

¹ Institute of Materials Research, German Aerospace Center, Linder Höhe, 51147 Köln, Germany

² Institute for Inorganic and Analytical Chemistry, Justus-Liebig-Universität Gießen, Heinrich-Buff-Ring 58, 35392 Gießen, Germany

^{a)} Author to whom correspondence should be addressed: severin.kopatz@dlr.de

ABSTRACT

A high thermoelectric (TE) figure of merit zT of materials enables a high energy conversion efficiency. The quantity zT is defined by the Seebeck coefficient (S), the electric (σ) and thermal (κ) conductivity, and the absolute temperature (T). In this paper, we report on a computational model of the Combined ThermoElectric Measurement (CTEM) apparatus, which is a simultaneous characterization method capable of measuring the full set of above-mentioned thermoelectric transport properties between -190 and 600°C . Currently, the measurement results show deviations due to unidentified error sources. As a solution approach of identifying possible error sources, a digital twin of the CTEM was developed. The computational thermal-electrical circuit model mainly consists of thermal sieving chains representing the relevant sample holder components, in particular two metallic blocks and a TE sample. For a computational consistency check of the measuring principles, ideal conditions are assumed, while no potential error sources are implemented, yet. Here, we present the measurement principles and procedures of creating the computational model of the CTEM. After studies on local discretization, the computational model undergoes a consistency check for model validation. The deviations between input parameters and simulated results of the three mentioned thermoelectric properties have been found negligibly small ($\ll 1\%$) for ideal measurement conditions. This agreement certifies a realistic representation of the behavior of the sample holder by the digital twin with a satisfying reproduction of ideal measurement conditions by simplifying assumptions and the applicability of underlying measurement principles and evaluation protocols.

© 2023 Author(s). All article content, except where otherwise noted, is licensed under a Creative Commons Attribution (CC BY) license (<http://creativecommons.org/licenses/by/4.0/>). <https://doi.org/10.1063/5.0129504>

I. INTRODUCTION

Thermoelectric (TE) materials can reversibly transport heat, and by that, they have the possibility to transform heat into electricity and vice versa.^{1–3} That means that if a temperature difference is applied to a TE material, a voltage can be generated, and by applying the voltage to an isothermal TE material, heat can be transported and a temperature difference over the material is generated. Thermoelectric energy converters (thermogenators) use these features, and the key step for the optimization of them is the characterization of its efficiency η . The efficiency itself strongly depends on the figure of merit zT ,^{4–6} which is defined by the following equation:

$$zT = \frac{S^2 \sigma}{\kappa} T, \quad (1)$$

including the three thermoelectric transport properties, such as Seebeck coefficient S , electrical conductivity σ , and thermal conductivity

κ and the absolute temperature T . Commonly, the electrical conductivity and the Seebeck coefficient that together form the power factor^{5–7} of a sample are measured simultaneously in a custom-made measuring system (HT-S- σ ⁸ or ZEM⁹). On the other hand, the characterization of the thermal conductivity is often performed in a separate experimental setup (XFA,¹⁰ LFA,¹¹ and 3ω method¹² or other, steady-state methods¹³). Usage of several dissimilar methods could lead to several uncertainties regarding the accuracy of zT obtained by Eq. (1):

- If the same sample is measured successively in two different measuring systems, aging effects of the sample during temperature cycle can occur,^{14,15} effectively falsifying the specification of zT .
- If different geometries of the sample are necessary due to individual requirements of each experimental setup, two different samples need to be used for a full characterization.

These samples can be taken from different batches or can be separated from a single batch. Thus, either lacking reproducibility or any functional inhomogeneity can introduce a dissimilarity of thermoelectric properties.^{16–18} Therefore, characterizing one material by two samples can also cause a misinterpretation of the calculated zT .

Accordingly, a measurement system for the simultaneous investigation of all thermoelectric properties of a material will not provide the mentioned uncertainties. Furthermore, there can be more advantages using only one measurement system of a full characterization. Only one sample is necessary, which has to be synthesized and prepared; the sample has to be contacted and mounted just once; operation time and energy are saved as only one temperature cycle is necessary; and all properties are measured along the same axis of the sample, which is essential in the case of crystallographically anisotropic crystalline or textured materials. This type of measurement system has been already used for several materials, also in the temperature range below room temperature.^{19,20} As thermoelectric converter materials are often used to convert waste heat into electric energy in industrial or automotive applications,^{21–25} it is required to characterize thermoelectric materials in wide temperature ranges, which typically range from the room temperature up to 600 °C and beyond for thermoelectric generators. The device ALTEC10001, developed in the Institute of Thermoelectricity, Chernivtsi, Ukraine, is such a measurement system for measuring the three mentioned thermoelectric properties of material samples.²⁶ In the case of ALTEC10001, the characterization of the electrical conductivity and of the Seebeck coefficient provides sufficient accuracy. Possible error sources, which can have a certain influence on the accuracy of the results, appear only to a minor extent. On the other hand, several effects can disturb the measurement of thermal conductivity. Some of the relevant error sources are well known, generally.^{27–29} In the case of the thermal conductivity measurement by ALTEC10001, the effect of the thermal exchange between the sample and its environment via radiation has been investigated by means of a computational model³⁰ using the software tool COMSOL Multiphysics. The computational model is used not only to investigate the accuracy of the measurement, in general, but also to study faster measurement procedures for the determination of thermal conductivity³¹ and to finally reveal the methodical relation between the measuring rate and the achievable accuracy of the measurement in the presence of radiative effects.³² Computational models are very important tools to clarify the impact of experimental error sources and to find suitable ways for their compensation by the implementation of adapted measurement procedures and evaluation protocols.

This work is dedicated to the Combined ThermoElectric Measurement (CTEM) apparatus, which is a custom-made experimental setup for the characterization of thermoelectric materials. The CTEM provides an exact time resolution of the signals (e.g., temperatures, voltages, and currents) due to simultaneous capturing during a measurement, while the signals are recorded successively by using ALTEC10001. Additionally and redundant to the calculated figure of merit zT obtained by Eq. (1) from individual measurements of the constituting properties S , σ , and κ , it is possible to obtain the figure of the merit directly by the independent Harman measurement procedure.^{33,34} Similarly to ALTEC10001, the

measurement procedures of the CTEM for the electrical conductivity and Seebeck coefficient including data analysis provide highly accurate results. The characterization of the thermal conductivity by the CTEM includes the contribution of the thermal contact resistance between the sample and the attached metal blocks of the sample holder. Furthermore, the CTEM measurement is sensitive to several error sources of thermal nature, e.g., radiation coupling between the sample and the environment, or heat loss due to thermally conductive measuring probes and lead wires. The effect of these error sources is partially known from finite-element modeling (FEM) with the simulation tool ANSYS,²⁸ and consequently, correction terms are considered in the analysis to provide more precise results. In particular, the correction of radiative effects is already applied in the real experiment,²⁹ which allows for a reduction of deviations for the thermal conductivity measurement by ~30% to ~3% at the highest measurement temperature of 600 °C. For studying further possible error sources of the electrical conductivity and Seebeck coefficient measurement, a simplified network model of the real CTEM turned out to be very helpful. A digital twin, which is the virtual illustration of a real object using computational software tools, whether or not the object exists in the real world, saves resources since the implementation and testing of new components can be easily accomplished by digital counterparts, which effectively reduce the number of steps for the purchase, production or re-design of components, and the work associated with their installation into the experimental measuring setup. This particularly saves effort and time not only during early development phases but also for the improvement of the existing setups by investigations on the influence of geometries and material properties on measurement results or for studies on suitable means to minimize influences of a broad spectrum of possible error sources. The digital twin of the CTEM apparatus developed here is modeled using the software Scilab and its simulation tool Xcos. This software environment is very similar to the common software Matlab and its simulation tool Simulink. Several computational models of thermoelectric problems already exist,^{35–37} but they are not applicable to the CTEM. Therefore, a digital twin of the in-house built CTEM apparatus, including its measurement principles, will be a unique feature of its qualification. As a start, the digital twin should perfectly reproduce several input parameters, such as temperature-dependent functions of the thermoelectric properties, under ideal conditions without consideration of possible error sources. Second, disturbing effects, e.g., as are known from the literature²⁸ can be added to simulation, trying to reproduce erroneous experimental data. Additionally, the digital twin enables the investigation of complex combinations of uncertainties in various measured parameters. Thus, the identification of the acting spurious effect(s) is facilitated.

In the following, we present the measurement setup and principle of the in-house CTEM apparatus and its measurement procedures. Furthermore, the build-up of the digital twin is described and the results of the consistency check under ideal conditions are shown.

II. EXPERIMENTAL

A. Setup

The key element of the experimental setup is the assembly of the sample holder [Fig. 1(a)], which is inserted and fixed by two

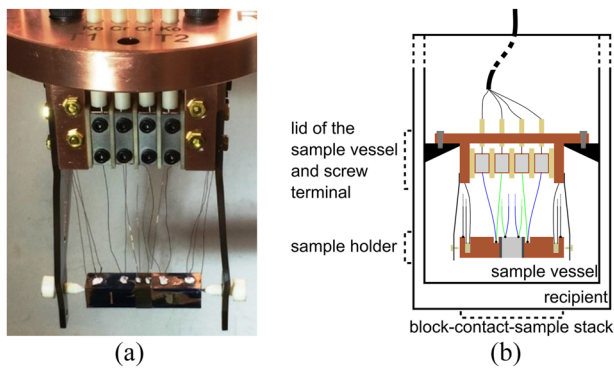


FIG. 1. Assembly of the sample holder in the CTEM. (a) Thermoelectric sample contacted by two metallic blocks via a soldering material. Each of the current supply lead and measuring cable is attached to either a block or the sample and to a block of the screwing terminal located above the sample holder. (b) Schematic sketch of the assembly, including the wiring and the thermal environment interacting with the sample.

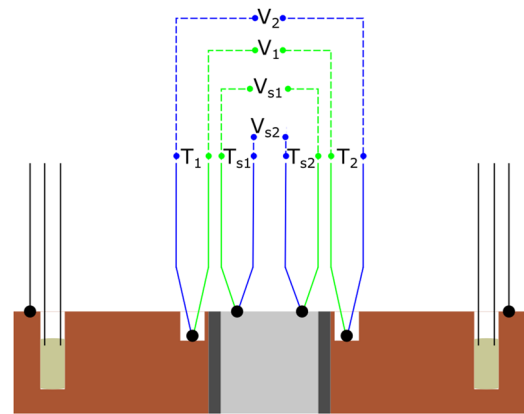


FIG. 2. Measuring circuits linked to the sample holder and attached thermocouples. Two types of voltage taps of the four thermocouples operate simultaneously. Besides the temperatures of the blocks T_1 and T_2 and the temperatures at the sample T_{s1} and T_{s2} , the voltage drops V_1 and V_2 , provided by the block potential probes and V_{s1} and V_{s2} and provided by the sample potential probes, are also recorded.

screws in a sample vessel. The vessel acts as desirably isothermal and temperature-controlled thermal environment. After mounting of the sample holder, the sample vessel is placed in a vacuum chamber (recipient) for the measurement. This compartment includes a type-K thermocouple for the control of the environment temperature by a proportional-integral-derivative (PID) temperature controller from Eurotherm.

The sample holder assembly can be divided in two parts: the lid of the sample vessel with the attached screw terminal and the sample holder.

The screw terminal consists of 14 electrically insulated copper blocks arranged in a horizontal rectangular pattern, with four blocks at the front and at the back and three blocks at the left side and at the right side of the screw terminal. The copper blocks are used as dismountable connection points for current and measuring signals from the sample holder. Fixed leads are installed from the screwing blocks to the feedthroughs of the recipient. The electric insulation between different channels within the screw terminal is accomplished by means of mica platelets [phlogopite— $\text{KMg}_3(\text{AlSi}_3\text{O}_{10})(\text{OH})_2$], which provide an insulating resistance of $> 10^{17} \Omega\text{cm}$ at 23°C and $> 10^{12} \Omega\text{cm}$ at 550°C .³⁸

The sample holder [Fig. 1(b)] uses a pair of leaf springs to apply a small compressive force along the block–contact–sample (bcs) stack in order to hold the configuration in place. The sample is placed between two identical metal blocks and is contacted to them by a solder material. Different species of solder materials are needed from case to case depending on the block material and the sample material, regarding its chemical compatibility to the material of the blocks, as well as of the sample.^{39,40} The cross section of the metallic blocks and the sample are identical. A current lead (for electrical conductivity and Harman measurement) and a small gradient heater (for Seebeck and thermal conductivity measurement) are attached to each block. Furthermore, there are four type E (chromel–constantan) thermocouples (TCs) attached to the assembly, one at each block and two on the sample, each of the latter located very close to the solder contact of either side of the sample (Fig. 2).

These TCs can work in two different modes simultaneously. On the one hand, each thermocouple provides a temperature measurement, which is accomplished by a read out of their thermovoltage. The temperatures of the blocks T_1 and T_2 are measured by the evaluation of thermovoltages VT_1 and VT_2 , whereas VT_{s1} and VT_{s2} are used to determine the temperatures at samples T_{s1} and T_{s2} . On the other hand, measurement loops, which are formed by the same type of the lead material of the two TCs, provide the voltage in between these sensing points, which is the thermovoltage between these points in the absence of an electric current. Accordingly, the TCs also act as potential probes and these circuits provide the signals V_1 and V_2 at the blocks and V_{s1} and V_{s2} for sensing points located at the sample under test. TCs at the sample additionally to those at the blocks have not been used previously with the CTEM²⁹ but represent a new feature of it. This modification opens the option to measure temperature and potential differences across the interface zones and by that enables characterization of thermal and electric contact resistances of the solder contacts.

The choice of suitable materials for the blocks and the solder depends on their electric and thermal properties and on their chemical compatibility. In the case of a solid contact material, a possible mismatch of thermal expansion coefficients with respect to the material of the sample and the blocks should be considered. Copper blocks are used due to their high electric and thermal conductivity in order to reduce resistive signal contributions by the blocks. Since copper can diffuse into many thermoelectric sample materials, especially at high temperatures,⁴¹ the solder should preferably act as a diffusion barrier too or should be complemented by a separate diffusion barrier. Common materials for the contacting solder are Galinstan³⁹ and Field's metal.⁴⁰ Although these solders do not suppress diffusion or intercalation of species totally, experiments with several thermoelectric material samples confirmed the formation of thin and stable intermetallic layers, which revealed a self-inhibiting behavior effectively limiting the growth of diffusion zones and their possible impact on the measurement.⁴⁰

B. Measuring principles

With the described setup, the thermoelectric properties of a sample are obtained by exploiting the following three measuring principles. The measurements are started under steady-state temperature conditions of the sample vessel T_{sv} and run sequentially:

- electrical conductivity (σ measurement),
- Seebeck coefficient and thermal conductivity (S - κ measurement, simultaneously), and
- Harman method to directly obtain the figure of merit zT_H .

1. Temperature stabilization

Before starting any measurement, the temperature of the sample vessel is stabilized first to achieve steady-state temperature

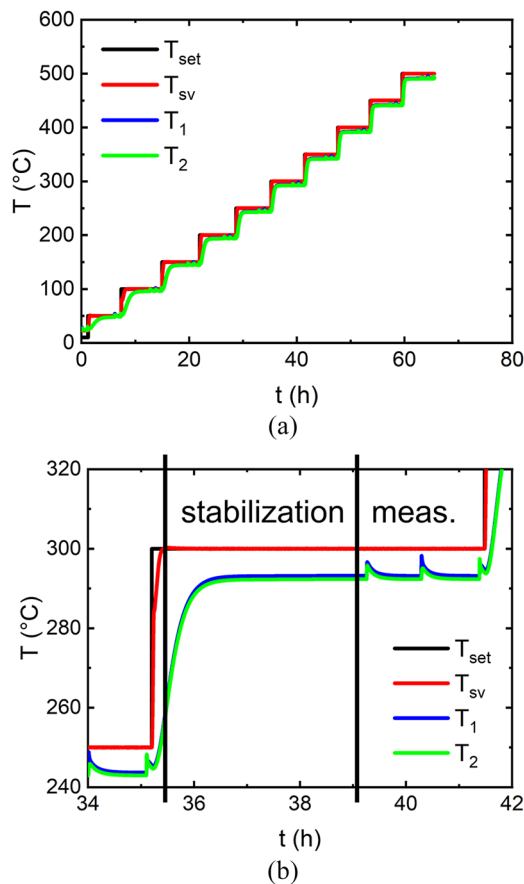


FIG. 3. Temperature evolution during a CTEM measurement cycle. (a) Thermal history over the whole ascending period of the measurement cycle. (b) Zoom on the temperature stabilization at a set point of 300 $^{\circ}\text{C}$ (labeled as “stabilization” range). The black curve represents the setpoint value T_{set} of the controller, the red curve represents the temperature of the sample vessel T_{sv} , the blue and green curves represent the block temperatures of the sample holder. The temperature peaks during the measurement (labeled as “meas.” range) following the stabilization phase are linked to the periods when the gradient heaters in the holder blocks are operated.

conditions. The temperature of the sample holder, represented by the temperatures T_1 and T_2 , follows passively. A temperature set-point value T_{set} is set for the sample vessel and controlled by the Eurotherm temperature controller, which is connected to an additional TC located at a sample vessel wall providing its actual local temperature (Fig. 3).

The temperature of the sample vessel reaches the target value quickly, while the temperature of the sample holder follows slowly constrained by the heat transfer from the vessel to the holder by thermal radiation. The final temperature of the sample is lower than the temperature of the vessel. The most probable explanation of the remaining difference between T_{sv} and the sample temperature is that the assembly of the sample holder does not see an isothermal environment as intended, especially that the vessel lid has a poor thermal connection to the sample vessel [Fig. 1(b)]. Additionally, the lid of the vessel is thermally facing the top of the recipient, which is connected to the laboratory and has nearly a room temperature of about 20 $^{\circ}\text{C}$. Therefore, the measuring head is slightly colder than the sample vessel. The thermal coupling between the vessel lid and the sample vessel or rather the top of the recipient and the resulting temperature profile within the sample vessel has not been fully monitored, yet. Preliminary tests with provisional fixation of thermocouples at the terminal block indicate a vertical and lateral temperature difference in the range of 10 K. After the sample has reached its final temperature, the system is kept for a certain stabilization time to fully ensure steady-state temperature conditions of all components of the measuring system.

2. Electrical conductivity measurement

An alternating current (AC) is applied to the sample by an external power supply for the measurement of the electrical conductivity. Prevention of Peltier heat transport, which would otherwise cause parasitic thermovoltages between the joints of dissimilar materials within the measuring circuit (in particular at the sample), is accomplished by the application of a sufficiently high current frequency > 10 Hz. For higher frequencies, noise signals will be intensified, which could impair the signal-to-noise ratio and therefore affect the signal acquisition. All signals are captured by using a transient recorder (“GEN3t” from the company Hottinger, Brüel & Kjær) with a sampling rate of 10 kHz. Prior to amplification by the transient recorder, signals are filtered by using a low pass filter with a frequency of 500 Hz. The current frequency is set to 127.2 Hz in order to avoid interferences with the power line frequency of 50 Hz. The sample current is measured by using a voltage drop over a shunt resistor ($0.1 \pm 0.001 \Omega$), which is connected in series to the sample holder and located outside the recipient in a thermally dammed box to prevent deviations due to temperature fluctuations. The voltage drop across the sample is measured by either the signal V_{s1} or V_{s2} . The amplitudes of the current I and the sample voltage drop V are determined by a Fourier analysis of the signals, which are captured by the transient recorder. Knowledge of the sample’s geometry and both amplitudes gives access to the electrical conductivity of the sample σ_s , which is calculated under the assumption of a one-dimensional (1D) current flow through the configuration as

$$\sigma_s = \frac{d}{A_s} \frac{I}{V_{si}}, \quad i = 1 \text{ or } 2, \quad (2)$$

with the distance of the sample TCs d and the cross section A_s of the sample. The distance of the sample TCs is obtained by preceding measurements after sample installation by means of a caliper, and it is in the range of 5 mm. Since the sample TCs are welded manually to the sample, d is not a constant value for every sample installation but has to be measured each time and prior to the start of the measurement. Moreover, it is very difficult to identify the exact distance of the sample TCs due to the geometric extension of the contact points ($\Delta d \approx \pm 10\%$), which finally yields deviating results of the sample's electric conductivity compared to literature or reference values. Another way of obtaining the sample's electrical conductivity is the usage of the voltage drop between the block TCs V_1 and V_2 . The electric resistances of the block and the contact material are very low compared to the resistance of the sample. Thus, neglecting these contributions, the electrical conductivity of the sample σ_b provided by the block TCs is approximated by

$$\sigma_b = \frac{l_s}{A_s} \frac{I}{V_i}, \quad i = 1 \text{ or } 2. \quad (3)$$

Here, l_s denotes the total length of the sample. Systematic deviations between σ_s and σ_b stem from the inherent electric contact resistances between the blocks and the sample and the contribution of the block resistance along the distance between the TC connection points and the sample interface. In the case of using a highly conductive metal as the block material (copper, nickel, or molybdenum), the electric resistance of the block R_b will be much smaller than the electric resistance of a typical TE material R_s ($R_b/R_s < 10^{-8}$) so that the resistive contributions of the blocks are negligible.

Another possible source of uncertainty is linked to the underlying definition of a one-dimensional (1D) measurement principle. The presented evaluation models assume a homogeneous current density over the block and sample cross sections throughout the sample holder configuration. This is ensured only by a uniform contact quality between the blocks and the sample and by a functional homogeneity of the sample material. The control of the contacting step and the application of the solder material to reproducibly reach low electrical and thermal contact resistance are very relevant for a correct measurement, as described in a previous study.⁴⁰

3. Measurement of Seebeck coefficient and thermal conductivity

By applying a constant output to one of the gradient heaters, the Seebeck coefficient and the thermal conductivity are obtained simultaneously by the analysis of the exponential decay of the occurring temperature difference after switch-off. Hereby, the heating power of the gradient heater should be large enough to create the temperature difference over the sample of a few Kelvin in a short time of some seconds. A thermovoltage is generated along the sample in response to this temperature difference. The total thermovoltage of the measuring circuit, including the contributions of the signal paths, is tapped by both potential probes of the sample, providing the voltages V_{s1} and V_{s2} (Fig. 4).

The total thermovoltages V_{s1} and V_{s2} are captured simultaneously and given by

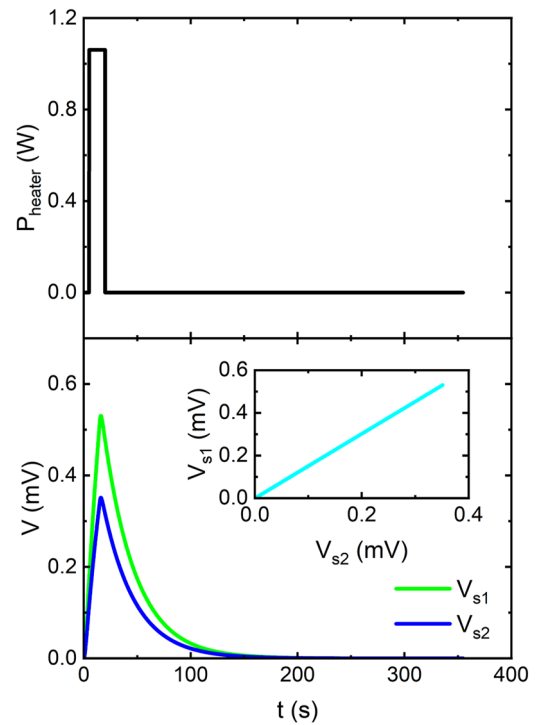


FIG. 4. Signals during the S- κ measurement. The thermal excitation is accomplished by a voltage pulse, which is applied to the resistance heater (graph on the top). The lower panel represents the thermovoltages V_{s1} and V_{s2} , which are used to calculate the Seebeck coefficient and the thermal conductivity and monitor the evolution of thermovoltages V_{s1} and V_{s2} , which reflects the build-up and relaxation of the temperature difference over the sample. The inset shows the linear relation between V_{s1} and V_{s2} .

$$V_{s1} = - \int_{T_{s1}}^{T_{s2}} dT [S_s(T) - S_1(T)] \approx -[S_s(\bar{T}) - S_1(\bar{T})](T_{s2} - T_{s1}), \quad (4)$$

$$V_{s2} = - \int_{T_{s1}}^{T_{s2}} dT [S_s(T) - S_2(T)] \approx -[S_s(\bar{T}) - S_2(\bar{T})](T_{s2} - T_{s1}), \quad (5)$$

with the Seebeck coefficient of the sample S_s and the Seebeck coefficients of both wire materials of the TCs S_1 and S_2 , which are taken from the literature.⁴² For a sufficiently small temperature difference, the average temperature $\bar{T} = \frac{1}{2}(T_1 + T_2)$ can be used for the calculation of the Seebeck coefficients. In the case of obtaining the Seebeck coefficient of the sample S_s , the equations of V_{s1} and V_{s2} are combined to replace the temperature difference $\Delta T = (T_{s2} - T_{s1})$, which is equal in both Eqs. (4) and (5),

$$\frac{V_{s1}}{(S_s - S_1)} = \frac{V_{s2}}{(S_s - S_2)}. \quad (6)$$

After some transformations of Eq. (6), S_s is given by^{8,43}

$$S_s = \frac{S_{TC}(T)}{1 - a} + S_2(T), \quad (7)$$

with the differential Seebeck coefficient of the thermocouple $S_{TC}(T) = S_1 - S_2$ and the slope of the linear curve $a = \partial V_{s1}/\partial V_{s2}$, which is obtained by plotting both signals V_{s1} and V_{s2} against each other (inset of Fig. 4). The sample TCs should have a very good thermal coupling to the sample in order to minimize temperature differences between the sample and the sensing beads of the TCs. Chemical reactions of the TC materials with the sample should be avoided during the welding process, too, due to possible deviations from references of sensor characteristics. In the case of a parasitic thermal contact resistance of the two sample TCs and in the presence of an elusive heat flow along the sensing bead, the measured temperature difference will be misinterpreted (cold finger effect⁴⁴) and, therefore, the calculated Seebeck coefficient, too. Suppression of the cold finger effect can be achieved by thermal anchoring of the sensor cables very close to the measurement point (coiling the cables along an isothermal around the blocks or the sample) or by thermal anchoring at a temperature-stabilized base further away from the sample. In this case, the screw terminal represents the temperature-stabilized base, and it is roughly 10 cm above the sample holder [Fig. 1(b)].

The thermal conductivity is calculated from the relaxation time τ_1 of V_{s1} (of V_{s2}) during the decay phase of the temperature difference after switch-off of the gradient heater. The concept is based on the generalized Ioffe method⁴⁵ and is comparable to the electric analogy of a capacitor with capacitance C discharging over a resistance with its electrical conductance G . Here, the blocks represent the capacitor (heat reservoirs) and the sample in between describes the behavior of a low-pass (simple RC element) over which both heat reservoirs are balanced in the course of the relaxation process. The time dependent relaxation of the electric potential follows an exponential decay function according to a time constant $\tau = C/G$ in the electrical analogy. In the thermal domain, the relevant values are the heat capacities C_p and the thermal conductances K of the blocks and the sample, respectively. The formula of the thermal conductivity of the sample is obtained by considering the following basic concept (Fig. 5).

A temperature difference ΔT over the sample is already applied, and heat exchange between the bcs stack and its ambience is possible. In a first step, the temperature profiles $T_i(x, t)$ ($i = 1, 2, 3$), which are indices according to the individual components (Fig. 5), namely, of the sample and two blocks, have to be determined. The two blocks are completely identical, and they are made out of the same material and have the same geometry. Furthermore, the following initial conditions (i.c.) at $t = 0$ are applied:

$$T_1(x, 0) = T_{10}, \quad (8)$$

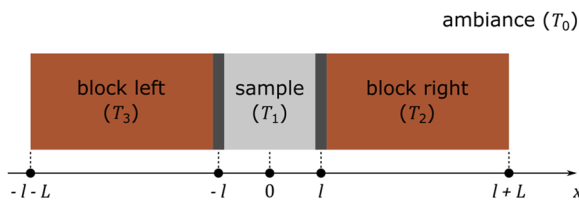


FIG. 5. Model of the bcs stack for the derivation of the formula of the sample's thermal conductivity.

$$T_2(x, 0) = T_{20}, \quad (9)$$

$$T_3(x, 0) = T_{30}. \quad (10)$$

A first set of boundary conditions (b.c.) is obtained by considering adiabatic conditions at the ends of the bcs stack ($x = l + L$ and $x = -l - L$),

$$\left(\frac{\partial T_2}{\partial x}\right)_{x=l+L} = 0, \quad (11)$$

$$\left(\frac{\partial T_3}{\partial x}\right)_{x=-l-L} = 0. \quad (12)$$

Furthermore, a continuous heat flow at the interfaces between the sample and each block ($x = l$ and $x = -l$) can be assumed as another set of b.c.,

$$\kappa_s \left(\frac{\partial T_1}{\partial x}\right)_{x=l-0} = \kappa_b \left(\frac{\partial T_2}{\partial x}\right)_{x=l+0}, \quad (13)$$

$$\kappa_s \left(\frac{\partial T_1}{\partial x}\right)_{x=-l+0} = \kappa_b \left(\frac{\partial T_3}{\partial x}\right)_{x=-l-0}, \quad (14)$$

with the thermal conductivity of the sample κ_s and of the blocks κ_b . On the other hand, at each of the inner interfaces, there is a temperature drop due to the presence of a thermal contact, which is represented by the soldering material,

$$T_1(l-0, t) = T_2(l+0, t) - \frac{\kappa_b}{K_c} \left(\frac{\partial T_2}{\partial x}\right)_{x=l+0}, \quad (15)$$

$$T_1(-l+0, t) = T_3(-l-0, t) - \frac{\kappa_b}{K_c} \left(\frac{\partial T_3}{\partial x}\right)_{x=-l-0}, \quad (16)$$

with the thermal conductance of the soldering material K_c . In a final step, the temperature profile within each component is subjected to Fourier's heat conduction law and the radiation law of Stefan and Boltzmann, regarding the thermal coupling to the ambience due to radiation. The ambient temperature T_0 is considered as constant during the whole steady-state temperature conditions,

$$C_{p,s} \frac{\partial T_1}{\partial t} = K_s \frac{\partial^2 T_1}{\partial x^2} - 4\sigma_{SB}\epsilon_s O_s T_0^3 (T_1 - T_0), \quad (17)$$

$$C_{p,b} \frac{\partial T_2}{\partial t} = K_b \frac{\partial^2 T_2}{\partial x^2} - 4\sigma_{SB}\epsilon_b O_b T_0^3 (T_2 - T_0), \quad (18)$$

$$C_{p,b} \frac{\partial T_3}{\partial t} = K_b \frac{\partial^2 T_3}{\partial x^2} - 4\sigma_{SB}\epsilon_b O_b T_0^3 (T_3 - T_0), \quad (19)$$

with the heat capacities $C_p = mc_p$, obtained by multiplying the mass m and the specific heat c_p ; the thermal conductances $K = \kappa \frac{A}{l}$, calculated by multiplying the thermal conductivity κ and the geometry factor; and the emissivity ϵ and the outer surfaces O of each component, respectively. The geometry factor is given by taking the inverse of the length l times the cross section A , while the latter is considered as equal for all components (blocks, contacting areas, and sample). In the case of using copper as a block material, the specific heat c_b

and the thermal conductivity κ_b are known from the literature.⁴⁶ The mass m_b and the length l_b of the block, as well as the mass m_s , the total length $l_s = 2l$, and the specific heat $c_{p,s}$ of the sample have to be measured beforehand. The general solutions of the temperature profiles T_1 , T_2 , and T_3 of the mentioned problem were obtained by a Laplace transform technique introduced by Doetsch⁴⁷ and already derived by Stecker and Teubner,⁴⁸

$$T_1(x, t) = T_0 + \sum_{n=1}^{\infty} [C_n e^{-P_n t} \cos(s_n x) + A_n e^{-M_n t} \sin(z_n x)], \quad (20)$$

$$T_2(x, t) = T_0 + \sum_{n=1}^{\infty} \{D_n e^{-P_n t} \cos[v_n(x - l - L)] + B_n e^{-M_n t} \cos[u_n(x - l - L)]\}, \quad (21)$$

$$T_3(x, t) = T_0 + \sum_{n=1}^{\infty} \{D_n e^{-P_n t} \cos[v_n(x + l + L)] - B_n e^{-M_n t} \cos[u_n(x + l + L)]\}, \quad (22)$$

with a set of coefficients C_n , P_n , s_n , A_n , M_n , z_n , D_n , v_n , B_n , and u_n , which can be obtained by introducing the aforementioned initial conditions and boundary conditions. For simplicity, the focus is on the exponential behavior of the temperature profiles $T_2(l, t)$ and $T_3(-l, t)$. Let the applied temperature difference ΔT be at symmetrically chosen positions $x = x_0$ and $x = -x_0$; consequently, ΔT can be calculated by the difference between Eqs. (21) and (22),

$$\begin{aligned} \Delta T &= T_2(x, t) - T_3(x, t) \\ &= 2 \sum_{n=1}^{\infty} B_n e^{-M_n t} \cos[u_n(x_0 - l - L)] \\ &\approx 2B_1 e^{-M_1 t} \cos[u_1(x_0 - l - L)]. \end{aligned} \quad (23)$$

For $n > 1$, all sum terms are smaller than 0.1% of the first term. The pre-factor u_1 is given by

$$u_1 = \frac{1}{l} \sqrt{\frac{\kappa_s \rho_b}{\kappa_b \rho_s}}, \quad (24)$$

with the material densities ρ . From Eq. (23), it is clearly seen that the temperature difference decays with a certain relaxation time $\tau_1 \equiv \frac{1}{M_1}$, as is also shown in Fig. 4, whereby the behavior of ΔT is represented by the thermovoltages V_{s1} and V_{s2} . The relaxation time τ_1 can be obtained by fitting an exponential decay function $V(t) = A e^{-\frac{t}{\tau_1}} + V_0$ to the thermovoltage signals in the time range after switch-off of the heater until the end of the measurement. The thermal conductivity of the sample κ_s scales with the inverse of the relaxation time τ_1 and can be expressed after some math as follows:²⁹

$$\kappa_s = \frac{l_s}{2A_s} \frac{m_b c_{pb}}{\tau_1} \left(1 + \frac{m_s c_{ps}}{6m_b c_{pb}} + \frac{2l_b k_s}{3l_s k_b} \right). \quad (25)$$

The formulation in the bracket represents a set of correction terms with respect to the block material. For simplicity (and for the consistency check of the digital twin under ideal conditions), the thermal coupling between the heated bcs stack and the ambiance due to radiative effects and the impact of the thermal resistance of the

soldering material are not considered here. However, the thermal resistance of the contacting is not negligible in the real-life CTEM apparatus. In particular, the interfaces within the bcs stack (block \leftrightarrow contact, contact \leftrightarrow sample) can affect the S - κ measurement due to changes of materials properties if the same bcs stack is measured several times where the thermal contact resistance of the solder contacting could vary from one to the next temperature cycle, which is not further investigated at this point.

4. Figure of merit

The efficiency of a thermoelectric generator strongly depends on the figure of merit zT of the employed thermoelectric legs. On the one hand, zT can be calculated via Eq. (1) with the knowledge of the aforementioned thermoelectric transport properties. On the other hand, zT can be also directly measured by the Harman method, which can be operated by the CTEM, yielding the henceforth called zT_H . By applying a direct current (DC) I through the sample, the sample potential probes immediately measure a voltage drop V_Ω due to the electric resistance of the sample. Concurrently to this ohmic voltage drop, the DC current yields an absorption and liberation of Peltier heat \dot{Q}_Π at both sample contacts, respectively, which is given by

$$\dot{Q}_\Pi = (\Pi_s - \Pi_{cs})I = (S_s - S_{cs})TI, \quad (26)$$

with the Peltier coefficients $\Pi_i = S_i T$, obtained by the product of the temperature T and the Seebeck coefficient of the sample S_s and of the material of the current supply wire S_{cs} . A temperature difference ΔT establishes over the sample as a reaction to this Peltier heat transport, which yields a transient thermovoltage contribution V_S to the measured voltage signal V_{s1} (Fig. 6). The temperature difference over the sample saturates once the Peltier-driven heat flow equals the back flow through the sample by Fourier transport \dot{Q}_F and residual thermal bypasses. The Fourier heat flow through the sample is obtained by

$$\dot{Q}_F = \frac{A_s}{l_s} \kappa_s \Delta T, \quad (27)$$

with A_s and l_s being the cross section and the length of the sample. Once the temperature difference stabilizes and with the neglect of thermal bypasses, the thermal equilibrium is given by the balance between Peltier heat and Fourier heat,

$$(S_s - S_{cs})TI = -\frac{A_s}{l_s} \kappa_s \Delta T, \quad (28)$$

and thus, the temperature difference over the sample can be expressed by

$$\Delta T = -\frac{l_s}{A_s} \frac{(S_s - S_{cs})}{\kappa_s} TI. \quad (29)$$

The temperature difference can be substituted in Eq. (4), which describes the obtained thermovoltage measured by the potential probes,

$$V_S = \frac{l_s}{A_s} \frac{(S_s - S_1)(S_s - S_{cs})}{\kappa_s} TI. \quad (30)$$

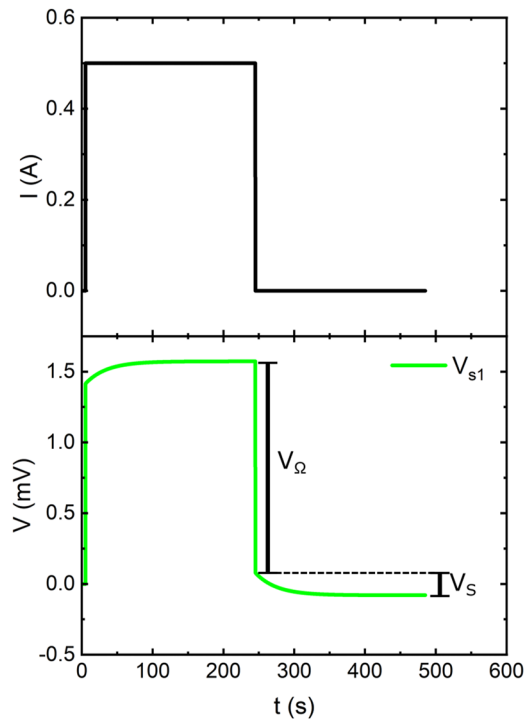


FIG. 6. Signals during the Harman measurement. It shows the signals from which zT can be directly measured as zT_H . A DC current pulse function is applied through the bcs stack (graph on the top). The occurring voltage signal consists of an ohmic voltage drop and concurrent development of a thermovoltage caused by the Peltier-driven temperature difference (graph on the bottom).

Introducing the ohmic voltage drop $V_\Omega = \frac{I}{A_s} \frac{l}{\sigma_s}$ yields the following expression of the voltage signal V_S :

$$\begin{aligned} V_S &= \frac{(S_s - S_1)(S_s - S_{cs})\sigma_s}{\kappa_s} T V_\Omega \\ &= \frac{S_s^2 \sigma_s}{\kappa_s} T \left(1 - \frac{S_1}{S_s}\right) \left(1 - \frac{S_{cs}}{S_s}\right) V_\Omega \\ &= zT \left(1 - \frac{S_1}{S_s}\right) \left(1 - \frac{S_{cs}}{S_s}\right) V_\Omega. \end{aligned} \quad (31)$$

By transformation of this equation, the Harman figure of merit is obtained,

$$zT_H = \frac{V_S}{V_\Omega} \left[\left(1 - \frac{S_1}{S_s}\right) \left(1 - \frac{S_{cs}}{S_s}\right) \right]^{-1}, \quad (32)$$

whereas the thermovoltage signal V_S is set to the value subsequent to the ohmic voltage drop, which is achieved after turning off the current. It has to be mentioned that it is very important to reach thermal equilibrium before the current is switched off in order to measure the full thermoelectric voltage V_{s1} and not to underestimate zT_H .

III. SIMULATION

A simulation tool for studying thermoelectric systems should include electrical and thermal components and thermoelectric elements to cover coupled effects of both physical domains. The Modelica language, which was introduced by Elmqvist and Mattsson in 1997,⁴⁹ is very suitable for this purpose since its library contains many physical components, such as electric resistors, capacitors, thermal conductors, heat capacitors, sensors, and sources of current, voltage, and heat,⁵⁰ and was already used to simulate thermoelectric problems.^{21,25,51} It is an equation-based language, which allows for an implementation of user-defined functional elements. The numerical software Scilab/Xcos is using the Modelica language, which enables the simulation of a 1D network model of the experimental CTEM setup. In considering time notations of Xcos, the duration of a simulated measurement principle t_{sim} from a starting point t_{start} to a final point t_{end} is called “final integration time.” Additionally, the time stepping Δt of simulation, which is the time in seconds between two output events, is named “period.” The elements of the computational model should fulfill the following requirements:

- possibility of simulating the thermoelectric effects Joule heating, Seebeck effect, and Peltier effect. The Thomson effect will not be considered due to the fact that the temperature difference over the sample is very small in the CTEM, and consequently, the spatial gradient of the Seebeck coefficient does not contribute significantly to the heat balance;
- implementation of temperature dependent material properties $f_i(T)$ ($i = \sigma, S, \kappa$, and c_p);
- possibility to connect electric and thermal equivalent circuits for the representation of user-defined thermoelectric effects (Fig. 8); and
- availability of control functions for a user defined setting or automated selection of material properties, experimental details, and boundary conditions within the simulation workflow (Sec. II B).

The toolbox Coselica, which was already developed and published for Scilab/Xcos,⁵² includes thermal components, which can be tuned as well,⁵³ but none of the other requirements are fulfilled. Therefore, new self-made elements were added to the component library of Xcos to enable the development of a digital twin of the CTEM. In a first step, a simple computational model of the CTEM sample holder without consideration of error sources (e.g., non-ideal contacts, heat exchange from or to the sample holder by thermal radiation) enables a consistency check of the implemented measurement principles and determination of accuracy limits or deviations between input properties and simulated measurement results, respectively.

A. Structure

As a first approximation, the digital twin of the experimental CTEM consists of the above described bcs stack, which is the central element of the sample holder align with the above chosen denominations. Furthermore, potential electric and thermal short circuits within the screw terminal or thermal coupling to the ambient-like radiative heat transfer between the bcs stack and the sample vessel

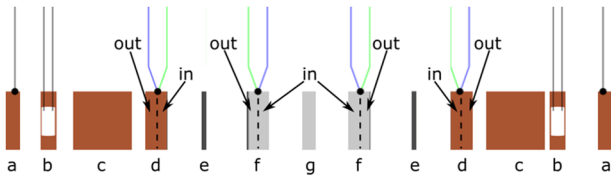


FIG. 7. Sections of the bcs stack. The model of the bcs stack is divided into different components: two blocks, two contact layers, and one sample. Except for the contact layer, all other components are divided into several sections, which reflect physical representations of different domains of the assembly with respect to locations of heaters and sensors.

are excluded so far. The bcs stack itself is composed of several parts (Fig. 7):

- edge section of the block with the connection point of the current supply (a),
- gradient heater section (b),
- middle section of the block (c),
- thermocouple section of the block that is equipped with a block TC and divided into inner [connected to (e)] and outer [connected to (c)] sub-sections (d),
- contact layer (e),
- thermocouple section of the sample that is equipped with a sample TC and divided into inner [connected to (g)] and outer [connected to (e)] sub-sections (f), and
- middle section of the sample (g).

A full equivalent thermoelectric circuit model (ECM) is built up for this configuration, which is the basic concept of the 1D network model of the CTEM (Fig. 8).

Temperature dependent material properties have been approximated by polynomial functions, which are stored in the

implementation files of respective components of the CTEM model. Depending on the measurement principle to be simulated and the starting temperature of the bcs stack $T(t_{\text{start}}) = T_{\text{start}}$, the model calculates the material properties automatically from these polynomials. There are two possible modes for calculating the properties. On the one hand and for simplicity, the material properties can be calculated at the very beginning of the simulation t_{start} and are kept constant until the end of the simulation t_{end} ,

$$f_i = f_i[T(t_{\text{start}})] = f_i(T_{\text{start}}) = \text{const.} \quad \forall t = [t_{\text{start}}, t_{\text{end}}]. \quad (33)$$

This case is designated as the constant mode (CM); the change of the properties with respect to temperature is not considered. Consequently, no disturbing effects on the simulated measurement results are expected by using the aforementioned measurement principles. A more realistic behavior of the material properties will be represented by the second calculation mode, the so-called non-constant mode (non-CM). For every time step Δt in between $[t_{\text{start}}, t_{\text{end}}]$ and for each section, the average temperature \bar{T} between the ends of it (o: outer, and i: inner) is calculated by

$$\bar{T}(t) = \frac{1}{2}[T_o(t) + T_i(t)], \quad (34)$$

and from that, the material properties are obtained,

$$f_i = f_i[\bar{T}(t)]. \quad (35)$$

This is very important in order to consider their temperature dependency in the case of temperature changes of the bcs stack during the simulation of different temperature settings and the thermal excitation by gradient heaters. Furthermore, each of the block [(a)–(d)], contact (e), and sample [(f) and (g)] sections of the ECM consists of a subgroup of elements, which reflect the local discretization (sieving chain) of the modeled part. This one-dimensional

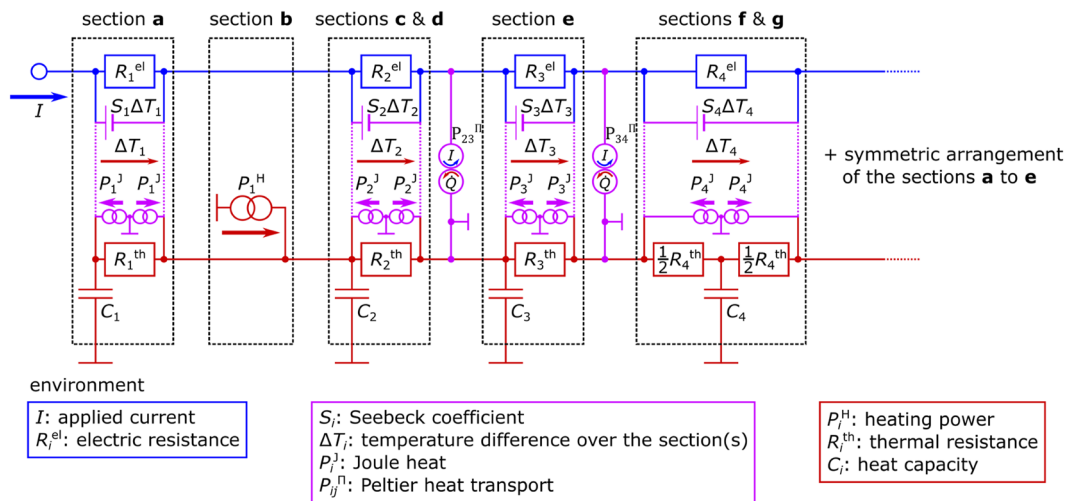


FIG. 8. Fully thermoelectric circuit of the bcs stack. The blue path defines electric elements of the equivalent circuit, mainly ohmic resistances. The current source is installed outside of the recipient. The red path represents thermal elements, such as thermal resistances and heat capacities. The purple paths contain self-defined elements implementing thermoelectric effects and representing resistive heaters, sources of thermovoltages (Seebeck), and heat (Peltier, Joule, and heater power).

discretization is necessary in order to achieve a correct reproduction of the physical behavior of the bcs stack, especially with respect to the spatially distributed heat capacity close to material transitions. The discretization will be particularly important in specifying precise temperature profiles during fast relaxation processes, e.g., after turning off an electrical current abruptly. Every element of the sieving chain contains a full set of relevant functional elements (resistances and heat capacities), which carry information about the underlying physical properties. In addition, it contains equations for the description of their electric, thermal, and thermoelectric behavior (Fig. 9). The input parameters and queries of the functional elements are defined as follows:

- n : numbers of sieving chain elements in the section; here, $n = 10$.
- sim_g_s_sc_m : geometry factor g of one sieving chain element of the middle section of the sample, $g = \frac{l_{\text{sec}}}{nA}$, with the length of the section l_{sec} .
- sim_T_start : starting value of the temperature T_{start} .
- sim_m_s_sc_m : mass of one sieving chain element of the middle section of the sample, $m = \frac{m_{\text{sec}}}{n}$, with the mass of the section m_{sec} .
- sim_mat_s : material of the TE sample, e.g., iron disilicide.
- sim_prop_type : keeping the transport properties f_i constant [CM, Eq. (33)] or temperature (time) dependency of the transport properties f_i during simulation [non-CM, Eq. (35)].

The gradient heater sections (b) contain voltage-controlled PT-100²⁹ resistive heating elements that release a heat flow of

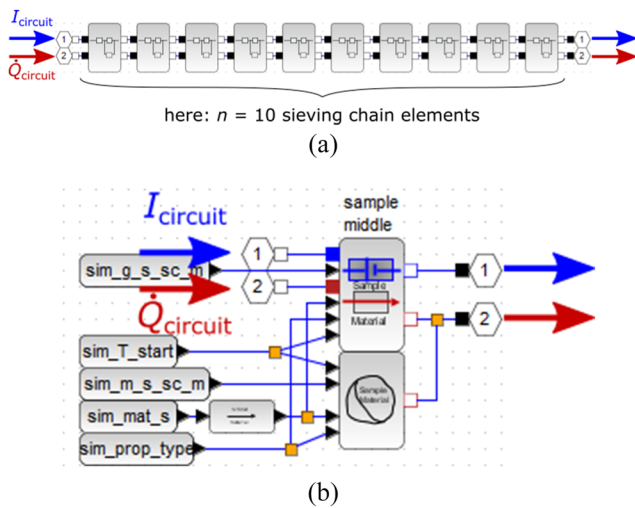


FIG. 9. Middle section of the sample. All sections of the bcs stack contain a certain number of sub-elements. Each of these elements includes input and output nodes for the electric current (blue) and heat flow (red) and a set of input parameters and queries of the physical components. The sub-elements are connected within a sieving chain. The physical behavior is reproduced by pre-defined heat capacitors (thermal inertia), thermal and electric resistances, and user-defined functional blocks for the representation of thermoelectric effects, such as the Seebeck and Peltier effects, respectively.

$\dot{Q} = UI = \frac{U^2}{R_{\text{PT-100}}}$. The Peltier effect at the interface between the block and the contact ($d \leftrightarrow e$) and at the interface between the contact and the sample ($e \leftrightarrow f$) is considered by Peltier heat sources, which absorb or release heat at the underlying sub-elements according to the following equation:

$$\dot{Q}_{\Pi} = (S_{m2} - S_{m1})TI. \quad (36)$$

S_{m1} denotes the Seebeck coefficients of the block or contact material and S_{m2} denotes the Seebeck coefficient of the contact or sample material, respectively, for the consideration of Peltier heat at two interfaces on each side of the bcs stack according to Fig. 8.

B. Simulation overview

In a first step, the described model is tested under ideal measurement conditions for a consistency check. This test is accomplished with the set of material properties of iron disilicide as input quantities of the CTEM model. Measuring principles and evaluation procedures were implemented into the digital twin in analogy to the experimental counterpart and have been simulated in order to validate the digital twin with respect to its functionality and correctness of simulated measurement results. In addition, the validity of simplifying assumptions in the thermal conductivity measurement can be judged from the coincidence of the simulated measurement result to the input value. The process from executing simulation to obtaining the results of the simulated data is shown in Fig. 10.

The first step is the implementation of the parameters for the simulation control, initial conditions, and provision of material and geometry data, which include the following:

- experiment type: σ , S - κ , or Harman measurement;
- time settings: duration (final integration time) and time stepping (period) of simulation;
- temperature settings: set of starting temperatures T_{start} to be simulated;
- source properties: amount of output, which is applied to the current source or to the gradient heater(s) and selection of side from which current or heat is applied to the bcs stack;
- selection of materials: block, contact, and sample; and
- bcs stack component properties: mass and geometry.

Reference data of the thermoelectric transport properties of the iron disilicide compound sample are taken from other in-house measuring systems (HT-S- σ and XFA). Highly conductive copper is used for the blocks and soldering material ($\hat{=}$, no soldering material), whose properties are taken from the literature.⁴⁶ A set of starting values for the temperature T_{start} is selected, which specifies the temperature range of the simulated characterization by the digital twin. The stabilization period of the experiment is not considered by simulation. Simulation is rather executed after stabilization by starting from constant temperatures T_{start} sequentially, assuming each time a homogeneous temperature distribution over the bcs stack at the beginning. Following all measurements at a temperature point, the obtained values (temperatures and voltage signals) are stored in matrices, which are exported to data files. These files have the same data format as the real CTEM experiment, which facilitates a direct comparison.

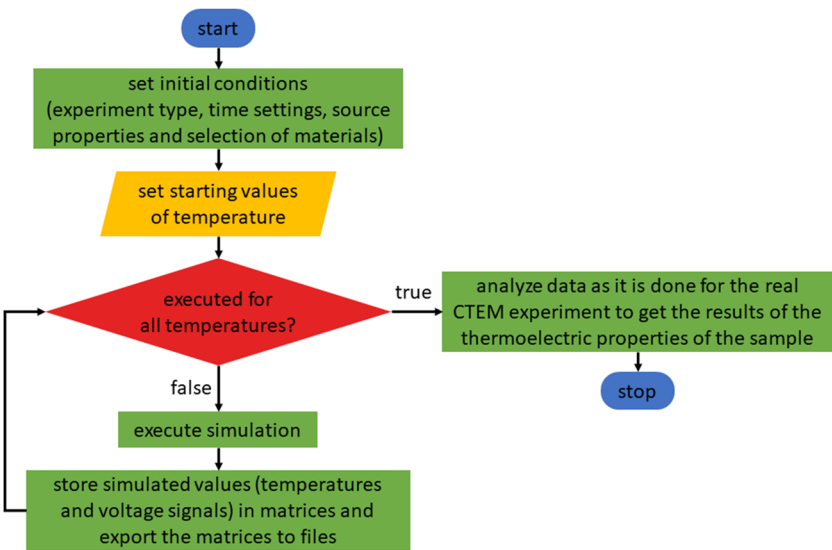


FIG. 10. Flowchart of simulation of a CTEM measurement in dependence on temperature.

C. Impact of local discretization of elements in the sieving chain

A reasonable number of elements in the sieving chains of individual components (Fig. 9) are a relevant aspect for the computational model. The aim is to find a configuration, which provides very low deviations on the one hand and saves computation time on the other hand. This kind of local discretization plays a crucial role in any kind of physical simulation, for example, in simulating the thermal conductivity, which mainly covers heat capacity effects here. The underlying heat equations consist of three partial

differential equations (PDEs), namely, the ones of the sample and of both blocks, respectively [see the derivation of κ_s , Eqs. (17)–(19)]. In doing so, the derivatives of the temperature (with respect to space and time) are transferred into temperature differences and the related differential equations are converted into systems of linear equations. The question, therefore, is how the extensive quantities (heat capacities and conductances) of a certain sieving chain section change with respect to the temperature range, defined by the applied temperature difference and by varying the length of the section. In the case of simulating the measurements of the electric

TABLE I. Number of elements in the sieving chains of the middle section and the thermocouple sections of the sample. This table shows the number of sieving chain elements n_{ele} of all of the five sample's sections [2× inner and outer sub-section of the thermocouple sections (f) and 1× middle section (g)]. Additionally, the average computation time t_{com} per temperature step is given and the average relative deviation $\Delta\kappa_{av}$ between simulated results and input data is presented.

Config. Number	Middle section	Thermocouple section		t_{com} (s)	$\Delta\kappa_{av}$ (%)
	n_{ele}	n_{ele}			
1	1	1		95	+0.788
2		2		120	+0.769
3		3		135	+0.763
4		4		155	+0.760
5		5		185	+0.758
6	2			120	+0.088
7				120	−0.257
8				135	−0.374
9				140	−0.429
10				155	−0.461
11		2		230	−0.533
12				390	−0.562
13				580	−0.574
14				865	−0.580
15				1115	−0.581

29 January 2024 06:28:47

TABLE II. Properties of the bcs stack components.

Component	Section	Parameter	Value
Each	All	Cross section	64 mm ²
	All	Density	8.938 · 10 ⁻³ g/mm ⁻³
Block	Edge section (a)	Length	0.5 mm
	Middle section (c)	Length	15 mm
	Subsections (inner and outer) of thermocouple section ($\frac{1}{2}$ d)	Length	0.25 mm
Contact	All	Density	7.880 · 10 ⁻³ g/mm ⁻³
	Total (e)	Length	0.01 mm
	All	Density	4.800 · 10 ⁻³ g/mm ⁻³
Sample	Subsections (inner and outer) of thermocouple section ($\frac{1}{2}$ f)	Length	0.5 mm
	Middle section (g)	Length	2.5 mm

conductivity and the Seebeck coefficient, the temperature difference over the bcs stack or over a certain sieving chain section of it is either zero (σ measurement) or very small (S measurement). The local temperature dependence of σ and S is also very small within the given temperature range. Therefore and with respect to the CTEM conditions, these two properties can be generally accumulated in a few or rather in one sieving chain element without loss of accuracy between input values and simulated measurement results. On the other hand, a fine local discretization is inevitable in simulating the measurement of the thermal conductivity even though the temperature difference is small since it is measured by a transient method and, therefore, is affected by the heat capacity of the sample. This is due to the fact that the heat stored in the sample is compensated during the relaxation process. Consequently, temperature gradients accumulate, which acts like an increase of the thermal resistance of the sample. In the following, the deviation $\Delta\kappa$ between simulated measurement results κ_{sim} and input values κ_{in} is investigated for the thermal conductivity for different settings of the local discretization of sample sections (Table I) and $\Delta\kappa$ at each temperature is calculated via

$$\Delta\kappa = \left(1 - \frac{\kappa_{\text{sim}}}{\kappa_{\text{in}}}\right). \quad (37)$$

An average deviation $\Delta\kappa_{\text{av}}$ of each configuration and for all of the seven starting temperature values (STV) is obtained by

$$\Delta\kappa_{\text{av}} = \frac{1}{7} \sum_{STV=1}^7 \Delta\kappa_{STV}, \quad (38)$$

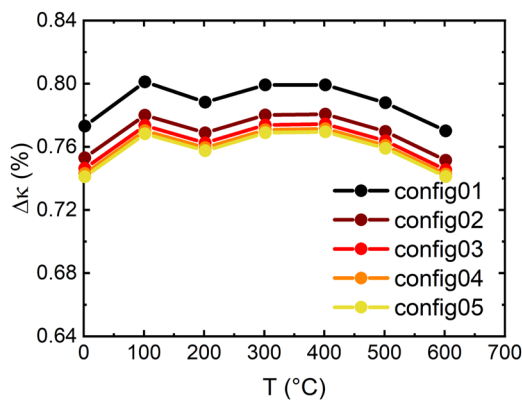


FIG. 11. Deviation of the thermal conductivity for sieving chain configurations 1–5. It shows the resulting temperature-dependent deviations of the simulated measurement of the thermal conductivity during tests for a single element in the middle section of the sample and the varying number of elements in the sample thermocouple sections.

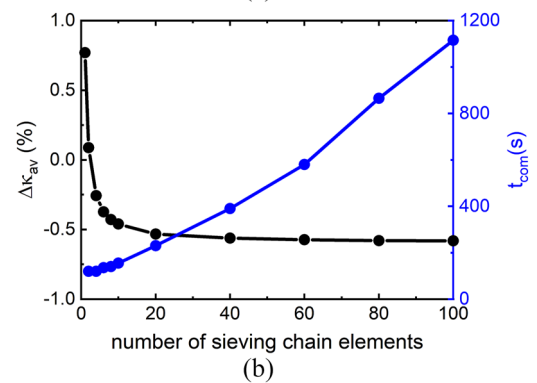
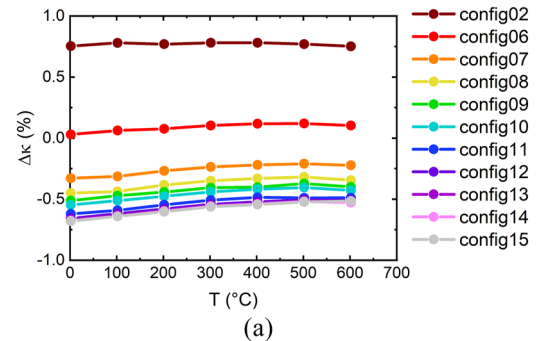
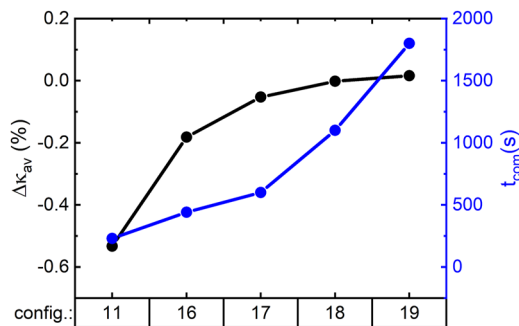


FIG. 12. Deviation of the thermal conductivity of iron disilicide for different sieving chain configurations. (a) Temperature-dependent deviations for a varying number of sieving chain elements in the middle section of the sample and two elements per thermocouple section. (b) Dependence of $\Delta\kappa_{\text{av}}$ and of t_{tot} with respect to the number of sieving chain elements in the middle section of the sample.

TABLE III. Number of elements of the sieving chains of the middle section of the blocks.

Config. Number	Middle section n_{ele}	t_{com} (s)	$\Delta\kappa_{av}$ (%)
16	4	440	-0.182
17	10	600	-0.053
18	20	1100	-0.002
19	30	1800	-0.016

**FIG. 13.** Average deviation of the simulated κ and computation time with respect to the improved version of configuration 11.

with the deviation $\Delta\kappa_{STV}$ for a certain starting temperature from Eq. (37).

All sieving chains of other components of the bcs stack are represented by one subgroup of electric and thermal elements, as is shown in Fig. 9(b), and their properties are given in Table II.

Furthermore, the time stepping is set to 0.1 s ($\hat{=}$ 10 events per second) and the following initial and boundary conditions are equal for all simulations:

- initial conditions: the whole bcs stack is isothermal at T_{start} ;
- boundary conditions: no heat flow from the bcs stack to the environment (no environment is considered in the model yet) and ideal heat transfer at the interface between all neighboring sections (no thermal contact resistances considered yet).

In configurations 1–5, the middle section of the sample is represented by one sieving chain element, while the number of those representing the sample's section close to the contact layer is varied. Indeed, varying the number of sieving chain elements of the thermocouple sections of the sample will not strongly affect the results of the thermal conductivity because these sections are smaller than the middle section of the sample. On the other hand, finding the optimal number of sieving chain elements of the thermocouple sections and setting the number of sieving chain elements of the middle section of the sample to 1 save computation time. The optimal number of the latter is found out afterward. The simulated measurement results for each of the configurations (1–5) are represented in Fig. 11.

TABLE IV. Full set of parameters and their values during the simulated measurements.

Parameter		Value		
Starting temperature values T_{start} (°C)		(0, 100, 200, 300, 400, 500, 600)		
Total simulation time t_{sim} (s)		σ meas. 2	S- κ meas. 360	zT_H meas. 365
Simulation period (time stepping) Δt (s)		σ meas. 0.0004	S- κ meas. 0.1	zT_H meas. 0.1
Block	Material	Copper		
	Total length (mm)	16		
	Total mass (g)	9.15		
	Number of sieving chain elements	Edge section (a) Middle section (c) Each TC section (d)	4 20 2	
Contact	Material	Copper		
	Total length (mm)	0.01		
	Total mass (g)	<0.01		
Sample	Material	Iron disilicide		
	Total length (mm)	4.5		
	Total mass (g)	1.38		
	Number of sieving chain elements	Each TC section (f) Middle section (g)	2 20	

Increasing the number of sieving chain elements in the thermoelement section from one to five (configurations 1–5) yields a moderate reduction for the deviation only, which seems to be not significantly reducible once these sections are discretized by more than five elements (configuration 5). With respect to the computation time, the second configuration (two sieving chain elements for the inner and outer sub-section of the thermocouple section) is chosen for further tests. In a next step, a number between two and 100 elements of the sieving chain is investigated for the middle section of the sample [configurations 6–15, Fig. 12(a)].

It is clearly seen that the usage of more elements of the middle section of the sample results in a saturation of the average deviation of κ , which is almost achieved for a number of sieving chain elements of 20 (configuration 11). However, $\Delta\kappa_{av}$ does not achieve zero deviation. As the thermal conductivity of the sample strongly depends on the heat capacity of the blocks [Eq. (25)], the local discretization of the individual sections of the blocks [edge (a), middle (c), and inner and outer thermocouple (d) sections, Fig. 7] needs to be considered similarly. The following simulations are done based on configuration 11 (20 subsections in the middle part) because the computation time is reasonable besides the saturation of deviation values at this point. For the improved version of configuration 11 (Table I), the sieving chain element length l_{sce} of sections (a) and (d) is set to 0.25 mm, the same value as the sieving chain element length of the outer sections of the sample (Table I). This yields four elements of the edge section of the blocks and two elements of the inner and outer thermocouple sections, respectively, which are held fixed for the following simulations. Therefore, only the number of sieving chain elements n_{ele} of the middle part of the blocks (c) is modified. The average time of computation t_{com} per temperature step and the average relative deviation $\Delta\kappa_{av}$ between simulated measurement results and input values are represented in Table III and Fig. 13.

By varying the number of sieving chain elements of the middle section of the blocks (Table III), the deviation between input values and simulated measurement results decreases in absolute values and closely approaches zero (black dots labeled configuration “16”–“19” in Fig. 13). Because the usage of 20 or 30 elements for the middle section of the block provides fairly accurate results and the deviation saturates close to zero, we assume that the usage of more elements will not affect the results strongly. With respect to computation time, configuration 18 is chosen for the simulation of a full characterization of iron disilicide, which provides the results for the consistency check of the digital twin. Further parameters are stored in Table IV.

Simulating the aforementioned procedures of the σ , S – κ , and Harman measurement provides very precise results with the usage of the settings presented here. The deviations Δp between input values p_{in} and simulated results p_{sim} for all properties are calculated similarly to Eq. (37),

$$\Delta p = \left(1 - \frac{p_{sim}}{p_{in}}\right), \quad p = \sigma, S, \kappa, \text{ and } zT_H. \quad (39)$$

An overview of the obtained values of each deviation Δp is shown in Table V, while the results of the thermoelectric figure of merit zT are represented in Fig. 14. To verify the simulated measurement

TABLE V. Overview of the deviations of the simulated thermoelectric properties σ , S , κ , zT_{calc} , and zT_H .

Quantity	Maximum value (%)
$\Delta\sigma$	$<5 \cdot 10^{-4}$
ΔS	$<3 \cdot 10^{-3}$
$\Delta\kappa$	$<2 \cdot 10^{-2}$
$\Delta(zT_{calc})$	$<6 \cdot 10^{-2}$
$\Delta(zT_H)$	<1.2

results of the thermoelectric figure of merit, a reference value zT_{ref} is calculated. In doing so, the temperature-dependent polynomials of the individual transport properties are inserted in Eq. (1) with the measuring temperature of the simulation T_{sim} ,

$$zT_{ref} = \frac{S(T_{sim})^2 \sigma(T_{sim})}{\kappa(T_{sim})} T_{sim}. \quad (40)$$

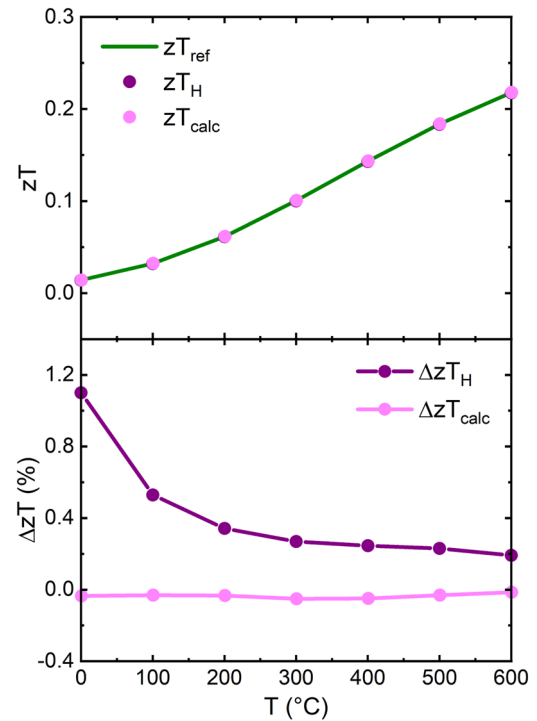


FIG. 14. Simulated measurement results of the thermoelectric figure of merit zT . In the upper panel, zT_H (marked in purple) represents the thermoelectric figure of merit, which is obtained by simulating the Harman measurement and using Eq. (32) for the analysis. zT_{calc} (marked as light magenta) denotes the thermoelectric figure of merit, which is obtained by inserting the results of the individual transport properties in Eq. (1). The deviation between zT_H and zT_{calc} with respect to a reference value zT_{ref} [upper graph, marked in green and obtained by Eq. (40)] is presented in the lower panel.

IV. CONCLUSION

The equivalent network model of the experimental CTEM apparatus, which is used to numerically simulate the characterization procedures for the determination of thermoelectric properties, has been presented. We described the underlying measuring principles and evaluation procedures, which are used in the real CTEM experiment. Furthermore, the development and the current implementation status of the digital twin have been shown, including important components to simulate the thermophysical behavior of the bcs stack under ideal measurement conditions. A consistency check between input datasets of material properties and simulated measurement results was accomplished for properties of an iron disilicide sample in the temperature range 0–600 °C. Investigations on the local discretization of individual components of the measuring configuration by the variation of the numbers of sieving chain elements revealed a dominating impact by the middle section of the sample and the sample holder blocks and confirmed that the sensitivity of simulated measurements results upon changes of these discretizations. However, the calculation of comparative property values from temperature-dependent characteristics of transport properties and their assignment as input parameters to locally discretized components of the simulated measurement configuration seem to represent a remaining source of deviation of the digital twin. Setting the discretization to 20 elements for the middle sections of the sample and the blocks yielded a minimum deviation of $2 \cdot 10^{-2}\%$ for the thermal conductivity. The deviations of S and σ did not depend on the number of sieving chain elements. For the electric conductivity, absolute values of the relative deviation are smaller than $5 \cdot 10^{-4}\%$ and, in the case of the Seebeck coefficient, smaller than $3 \cdot 10^{-3}\%$. Consequently, the figure of merit zT_{calc} calculated by the three properties can be obtained very precisely and the deviation with respect to a reference value zT_{ref} comprises approximately the sum of the individual deviations ΔS , $\Delta \kappa$, and $\Delta \sigma$ so that $\Delta zT_{\text{calc}} \approx \Delta S + \Delta \kappa + \Delta \sigma$. The results of the simulated Harman measurement are also very accurate. The maximum value of the deviation between zT_{H} and zT_{ref} is about 1% at a simulated measurement temperature of 0 °C, and the deviation decreases for higher temperatures. This can be explained as follows. On the one hand, the transient thermovoltage contribution V_S of the voltage signal is very low (cf. Fig. 6), and therefore, the calculated fitting functions are not always as accurate as possible, which could lead to uncertainties in the results of zT_{H} . On the other hand, the absolute values of zT_{H} and zT_{ref} are in a very good agreement, and the largest difference between them is smaller than $5 \cdot 10^{-4}$. However, due to the fact that the absolute value of zT_{H} is also very small (e.g., $1.394 \cdot 10^{-2}$ at 0 °C), the relative values of the deviations seem to be larger. Accordingly, the higher the absolute value of zT_{H} , the lower the deviations of the simulated zT_{H} . Therefore, there are no further investigations regarding the deviations between zT_{H} and zT_{ref} . Consequently, the presented computational model of the experimental CTEM apparatus is validated for iron disilicide. In a next step, a spectrum of TE materials with thermoelectric properties different from those of iron disilicide can be investigated to check the limitations of the digital twin with respect to the input temperature dependent functions representing the thermoelectric properties. Furthermore, potential error sources, such as radiative heat exchange or the presence of a soldering material with thermal and

electrical contact resistances, will be implemented within the digital twin in order to reproduce experimental behavior of the CTEM. The digital twin shall be used as a tool to check for the relevance and impact of individual error sources on measurement results in order to identify possible means for the reduction or compensation of their impact.

ACKNOWLEDGMENTS

The authors gratefully acknowledge the financial support from the DLR and thank Gregor Oppitz for his work on the hardware components and software development of the CTEM apparatus.

AUTHOR DECLARATIONS

Conflict of Interest

The authors have no conflicts to disclose.

Author Contributions

S. Kopatz: Conceptualization (lead); Data curation (lead); Formal analysis (lead); Visualization (lead); Writing – original draft (lead). **P. Ziolkowski:** Conceptualization (supporting); Supervision (equal); Writing – review & editing (equal). **E. Müller:** Conceptualization (supporting); Supervision (equal); Writing – review & editing (equal).

DATA AVAILABILITY

The data that support the findings of this study are available from the corresponding author upon reasonable request.

REFERENCES

1. T. M. Tritt, “Holey and unholey semiconductors,” *Science* **283**, 804–805 (1999).
2. F. J. DiSalvo, “Thermoelectric cooling and power generation,” *Science* **285**, 703–706 (1999).
3. H. Kleinke, “New bulk materials for thermoelectric power generation: Clathrates and complex antimonides,” *Chem. Mater.* **22**, 604–611 (2010).
4. G. Min, D. M. Rowe, and K. Kontostavlakis, “Thermoelectric figure-of-merit under large temperature differences,” *J. Phys. D: Appl. Phys.* **37**, 1301–1304 (2004).
5. H. S. Kim, W. Liu, G. Chen, C.-W. Chu, and Z. Ren, “Relationship between thermoelectric figure of merit and energy conversion efficiency,” *Proc. Natl. Acad. Sci.* **112**, 8205–8210 (2015).
6. J. He and T. M. Tritt, “Advances in thermoelectric materials research: Looking back and moving forward,” *Science* **357**, eaak9997 (2017).
7. M. Guch, C. Raj Sankar, J. R. Salvador, G. P. Meisner, and H. Kleinke, “Improvements of the thermoelectric properties of pbTe via simultaneous doping with indium and iodine,” *J. Appl. Phys.* **111**, 063706 (2012).
8. J. de Boer, C. Stiewe, P. Ziolkowski, T. Dasgupta, G. Karpinski, E. Lenz, F. Edler, and E. Mueller, “High-temperature measurement of Seebeck coefficient and electrical conductivity,” *J. Electron. Mater.* **42**, 1711–1718 (2013).
9. A. Riko, “Seebeck coefficient/electric resistance measurement system - ZEM-3 series,” <https://www.ulvac.com/userfiles/files/Components/Thermal-Analysis-and-Coating/Thermoelectric-Testers/ZEM-3.pdf>, Cat.No.ZEM-3_E_v3.1/16.01.0000.

- ¹⁰Linseis GmbH, XFA 600 Xenonflash Apparatus (Thermal Conductivity/Diffusivity, <https://pdf.directindustry.com/pdf/linseis-thermal-analysis/xf-600-xenonflash-apparatus-thermal-conductivity-diffusivity/30771-465307.html>).
- ¹¹NETZSCH-Gerätebau GmbH, LFA 467 HyperFlash® - Light Flash-Apparatur, <https://www.netzsch-thermal-analysis.com/de/produkte-loesungen/waerme-und-temperatur-leitfaehigkeitsbestimmung/lfa-467-hyperflash/l>.
- ¹²D. G. Cahill, "Thermal conductivity measurement from 30 to 750 K: the 3 ω method," *Rev. Sci. Instrum.* **61**, 802–808 (1990).
- ¹³D. Kraemer and G. Chen, "A simple differential steady-state method to measure the thermal conductivity of solid bulk materials with high accuracy," *Rev. Sci. Instrum.* **85**, 025108 (2014).
- ¹⁴R. Hara, S. Inoue, H. T. Kaibe, and S. Sano, "Aging effects of large-size n-type CoSb₃ prepared by spark plasma sintering," *J. Alloys Compd.* **349**, 297–301 (2003).
- ¹⁵L. Y. Herrera, A. Ruiz, H. Carreón, and V. H. López, "Application of the thermoelectric effect for monitoring aging effects on Inconel 600," *AIP Conf. Proc.* **2102**, 060007 (2019).
- ¹⁶A. Schmitz, C. Stiewe, and E. Müller, "Homogeneity of large thermoelectric samples produced by a short term sintering method," *SPP 1386 Winter School Bremen* (Bremen, Germany, 2010).
- ¹⁷S. Iwanaga and G. J. Snyder, "Scanning Seebeck coefficient measurement system for homogeneity characterization of bulk and thin-film thermoelectric materials," *J. Electron. Mater.* **41**, 1667–1674 (2012).
- ¹⁸N. Prasad, D. Nemir, J. Beck, J. Maddux, and P. Taylor, "Inhomogeneous thermoelectric materials: Improving overall zT by localized property variations," in *Energy Harvesting and Storage: Materials, Devices, and Applications VI* (SPIE, 2015), pp. 26–32.
- ¹⁹J. Chaussy, A. Guessous, and J. Mazuer, "Simultaneous measurements of thermopower, thermal conductivity, and electrical resistivity between 1.2 and 350 K," *Rev. Sci. Instrum.* **52**, 1721–1727 (1981).
- ²⁰H. Bougrine and M. Ausloos, "Highly sensitive method for simultaneous measurements of thermal conductivity and thermoelectric power: Fe and Al examples," *Rev. Sci. Instrum.* **66**, 199–206 (1995).
- ²¹M. Eschenbach, J. Ungethüm, and P. Treffinger, "Vehicle model for transient simulation of a waste-heat-utilisation-unit containing extended powertrain and fluid library components," in *5th International Modelica Conference* (The Modelica Association, Vienna, Austria, 2006), pp. 405–410.
- ²²K. Zorbas, E. Hatzikraniotis, and K. Paraskevopoulos, "Power and efficiency calculation in commercial TEG and application in wasted heat recovery in automobile," in *Proceedings from the 5th European Conference on Thermoelectrics, Odessa, Ukraine, 10–12 September 2007* (European Thermoelectric Society).
- ²³G. J. Snyder and E. S. Toberer, "Complex thermoelectric materials," *Nat. Mater.* **7**, 105–114 (2008).
- ²⁴B. Ismail and W. Ahmed, "Thermoelectric power generation using waste-heat energy as an alternative green technology," *Recent Pat. Electr. Eng.* **2**, 27–39 (2009).
- ²⁵T. Braig and J. Ungethüm, "System-level modeling of an ice-powered vehicle with thermoelectric waste-heat-utilization," in *Proceedings 7th Modelica Conference* (The Modelica Association, Como, Italy, 2009), pp. 708–715.
- ²⁶L. I. Anatyshuk, M. V. Havryliuk, and V. V. Lysko, "Absolute method for measuring of thermoelectric properties of materials," *Mater. Today: Proc.* **2**, 737–743 (2015).
- ²⁷J. de Boer and V. Schmidt, "Complete characterization of thermoelectric materials by a combined van der Pauw approach and the effect of radiation losses," *MRS Online Proc. Libr.* **1314**, 701 (2011).
- ²⁸K. Zabrocki, P. Ziolkowski, T. Dasgupta, J. de Boer, and E. Müller, "Simulations for the development of thermoelectric measurements," *J. Electron. Mater.* **42**, 2402–2408 (2013).
- ²⁹H. Kolb, T. Dasgupta, K. Zabrocki, E. Mueller, and J. de Boer, "Simultaneous measurement of all thermoelectric properties of bulk materials in the temperature range 300–600 K," *Rev. Sci. Instrum.* **86**, 073901 (2015).
- ³⁰L. I. Anatyshuk and V. V. Lysko, "Investigation of the effect of radiation on the precision of thermal conductivity measurement by the absolute method," *J. Thermoelectr.* **14**, 65–73 (2012).
- ³¹L. I. Anatyshuk and V. V. Lysko, "Increasing the rapidity of thermal conductivity measurement by the absolute method," *J. Thermoelectr.* **5**, 86–92 (2014). http://jt.inst.cv.ua/jt/jt_2014_05_en.pdf.
- ³²L. I. Anatyshuk and V. V. Lysko, "On improvement of the accuracy and speed in the process of measuring characteristics of thermoelectric materials," *J. Electron. Mater.* **43**, 3863–3869 (2014).
- ³³T. C. Harman, "Special techniques for measurement of thermoelectric properties," *J. Appl. Phys.* **29**, 1373–1374 (1958).
- ³⁴T. C. Harman, J. H. Cahn, and M. J. Logan, "Measurement of thermal conductivity by utilization of the Peltier effect," *J. Appl. Phys.* **30**, 1351–1359 (1959).
- ³⁵H.-L. Tsai and J.-M. Lin, "Model building and simulation of thermoelectric module using Matlab/Simulink," *J. Electron. Mater.* **39**, 2105–2111 (2010).
- ³⁶M. Singh, S. K. Bhukesh, and R. Vaishnav, "Modelling and simulation of solar thermoelectric generator," *J. Electr. Electron. Eng.* **10**, 71–76 (2015).
- ³⁷K. Kobbekaduwa and N. D. Subasinghe, "Modelling and analysis of thermoelectric generation of materials using Matlab/Simulink," *Int. J. Energy Power Eng.* **5**, 97–104 (2016).
- ³⁸Saveway Isolierstoffe GmbH, Technisches Datenblatt - SW-MICANITE FEST M & P, <https://www.saveway-isolierstoffe.de/de/produkte/elektrische-isolierstoffe/feste-glimmerplatten/duenne-glimmerplatten.html>, Revisionstand: 9.0 (2019).
- ³⁹H. Kolb, R. Sottong, T. Dasgupta, E. Mueller, and J. de Boer, "Evaluation of detachable Ga-based solder contacts for thermoelectric materials," *J. Electron. Mater.* **46**, 5057–5063 (2017).
- ⁴⁰A. Micallef, C. Stiewe, G. Oppitz, and E. Müller, "High-temperature specific contact resistance of iron disilicide soldered to molybdenum by field's metal," *ACS Appl. Electr. Mater.* **3**, 890–897 (2021).
- ⁴¹S. Asgary, M. R. Hantehzadeh, and M. Ghoranneviss, "Temperature dependence of copper diffusion in different thickness amorphous tungsten/tungsten nitride layer," *Phys. Met. Metallogr.* **118**, 1127–1135 (2017).
- ⁴²National Institute of Standards and Technology, NIST Standard Reference Database 60, <https://srdata.nist.gov/its90/download/download.html>, Version 2.0 (Web Version) (1993).
- ⁴³J. de Boer and E. Müller, "Data analysis for Seebeck coefficient measurements," *Rev. Sci. Instrum.* **84**, 065102 (2013).
- ⁴⁴J. Mackey, F. Dynys, and A. Schirlioglu, "Uncertainty analysis for common Seebeck and electrical resistivity measurement systems," *Rev. Sci. Instrum.* **85**, 085119 (2014).
- ⁴⁵A. V. Ioffe and A. F. Ioffe, "Measurement of the thermal conductivity of semiconductors in the vicinity of room temperature," *Sov. Phys.-Tech. Phys.* **3**, 2163–2168 (1958).
- ⁴⁶Jahm Software, Material Properties Database, <https://www.jahm.com/>, MPDB v7.39.
- ⁴⁷G. Doetsch, *Theorie und Anwendung der Laplace-Transformation*, 1st ed. (Springer, Berlin, Heidelberg, 1937).
- ⁴⁸K. Stecker and M. Teubner, "Untersuchungen verschiedener methoden der waermeleitsmessungen an halbleitern," *Wiss. Z. - Martin-Luther-Univ. Halle-Wittenberg, Math.-Naturwiss. Reihe XVI* 67 M(H. 1), 1 (1967).
- ⁴⁹S. E. Mattsson and H. Elmqvist, "Modelica - An international effort to design the next generation modeling language," *IFAC Proc. Vol.* **30**, 151–155 (1997).
- ⁵⁰Modelica Association, Modelica Contents, <https://build.openmodelica.org/Documentation/Modelica.html>.
- ⁵¹F. Felgner and G. Frey, "Object-oriented simulation model of thermoelectric devices for energy system design," in *2012 16th IEEE Mediterranean Electrotechnical Conference* (IEEE, Yasmine Hammamet, Tunisia, 2012), pp. 577–580.
- ⁵²D. Reusch, "Coselica toolbox - mehr als 200 modelica blöcke für scilab/xcos," Scilab Konferenz, 2014.
- ⁵³M. Łanczont, "Analysis of the possibilities to use coselica toolbox for simulate electrical circuits and heat flow," *Przegl. Elektrotech.* **1**, 31–34 (2017).